Eruption of Solar Magnetic Flux Ropes Caused by Flux Feeding

Quanhao Zhang[1,2,3,4] , Yuming Wang[1,3,4] , Rui Liu[1,3,5] , Jie Zhang[6] , Youqiu Hu[1], Wensi Wang[1,3,4], Bin Zhuang[1,4] , and Xiaolei Li[1,4]

[1] CAS Key Laboratory of Geospace Environment, Department of Geophysics and Planetary Sciences, University of Science and Technology of China, Hefei 230026, People's Republic of China; zhangqh@ustc.edu.cn
[2] State Key Laboratory of Space Weather, Chinese Academy of Sciences, Beijing 100190, People's Republic of China
[3] CAS Center for Excellence in Comparative Planetology, University of Science and Technology of China, Hefei 230026, People's Republic of China
[4] Mengcheng National Geophysical Observatory, School of Earth and Space Sciences, University of Science and Technology of China, Hefei 230026, People's Republic of China
[5] Collaborative Innovation Center of Astronautical Science and Technology, Hefei, Anhui 230026, People's Republic of China
[6] Department of Physics and Astronomy, George Mason University, 4400 University Drive, MSN 3F3, Fairfax, VA 22030, USA

Abstract

Large-scale solar eruptions are believed to have a magnetic flux rope as the core structure. However, it remains elusive as to how the flux rope builds up and what triggers its eruption. Recent observations found that a prominence erupted following multiple episodes of "flux feeding." During each episode, a chromospheric fibril rose and merged with the prominence lying above. In this Letter, we carried out 2.5-dimensional magnetohydrodynamic (MHD) numerical simulations to investigate whether the flux-feeding mechanism can explain such an eruption. The simulations demonstrate that the discrete emergence of small flux ropes can initiate eruptions by feeding axial flux into the preexistent flux rope until its total axial flux reaches a critical value. The onset of the eruption is dominated by an ideal MHD process. Our simulation results corroborate that the flux feeding is a viable mechanism to cause the eruption of solar magnetic flux ropes.

1. Introduction

Large-scale solar eruptions are manifested as the observed phenomena of flares, prominence/filament eruptions, and coronal mass ejections (CMEs). It is widely accepted that these kinds of events are intimately associated with a coronal magnetic flux rope system and are essentially different manifestations of the same physical process, i.e., the eruption of the rope system (Zhang et al. 2001; van Driel-Gesztelyi & Green 2015; Green et al. 2018; Jiang et al. 2018; Yan et al. 2018). A typical scenario is that, during a flux rope eruption, the prominence/filament contained in the rope also erupts with the rope, and the magnetic reconnection in the current sheet formed beneath the rope dramatically converts free magnetic energy in the coronal magnetic system into thermal energy and nonthermal particle acceleration, so that a flare occurs; this flux rope further propagates outwards and expands, so as to be observed as a CME in the corona and the interplanetary space (e.g., Lin & Forbes 2000). These large-scale eruptive activities are generally considered to be the major disturbance affecting the solar-terrestrial system (e.g., Shen et al. 2014). Therefore, it has great significance to study the formation process of an erupting magnetic flux rope and its trigger mechanism.

Various theoretical models have been proposed to investigate the eruptive mechanism of flux ropes, either based on magnetic reconnection (Antiochos et al. 1999; Chen & Shibata 2000; Moore et al. 2001; Sterling & Moore 2004; Archontis & Hood 2008; Inoue et al. 2015) or ideal MHD instabilities (Romano et al. 2003; Török & Kliem 2003; Kliem & Török 2006; Fan & Gibson 2007; Aulanier et al. 2010; Guo et al. 2010; Savcheva et al. 2012). It was also suggested by many authors that catastrophes could be responsible for solar eruptions: the onset of the eruption corresponds to a catastrophic loss of equilibrium (Forbes & Isenberg 1991; Isenberg et al. 1993; Lin et al. 2001; Chen et al. 2007; Démoulin & Aulanier 2010; Kliem et al. 2014a; Longcope & Forbes 2014). Flux rope catastrophes could be triggered by various physical processes. For example, it was found that there exists a critical value of the total axial (also called toroidal in a tokamak configuration) magnetic flux of a flux rope (e.g., Bobra et al. 2008; Su et al. 2009, 2011; Zhang et al. 2016, 2017a, 2017b; Zhuang et al. 2018). If the axial flux of the rope is smaller than this critical value, the rope system stays in equilibrium states; when this critical value is exceeded, loss of equilibrium occurs in the rope system: the flux rope jumps upward, with magnetic reconnection occurring below it, so that the rope erupts outward. This critical axial flux is of the order $10^{19} \sim 10^{20}$ Mx, and is influenced by various conditions, such as photospheric magnetic flux distributions (e.g., Zhang et al. 2017b).

Recently, it was observed by Zhang et al. (2014; hereafter Paper I) that a sequence of flux feeding episodes occurred within the two-day period prior to the eruption of a prominence. As shown in the right panel in Figure 1, a chromospheric fibril appeared as a dark structure at about 20 Mm along the slit before about 08:50 UT, after which it rose and merged with the prominence within about $40 \sim 60$ Mm along the slit. During a flux feeding process, magnetic flux and mass are injected into the target prominence from the chromosphere underneath. This is reminiscent of bubbles rising and expanding into quiescent prominences (e.g., Berger et al. 2010), as well as the transfer of magnetic flux and current between the different branches in a double-decker configuration (e.g., Liu et al. 2012; Cheng et al. 2014; Kliem et al. 2014b). As observed in Paper I, flux feeding events successively occurred three times, which increased the slow-
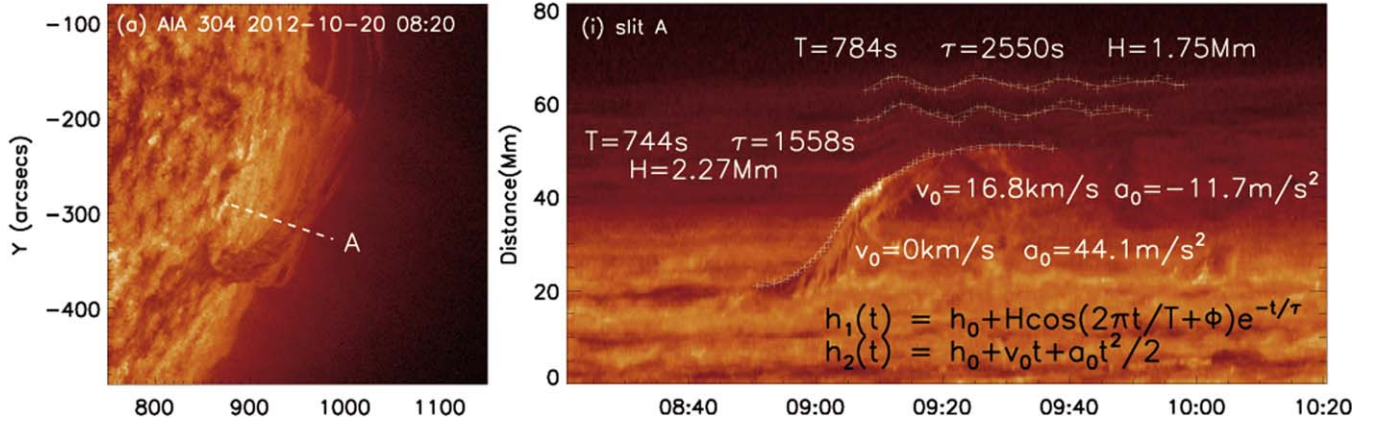
Figure 1. Observations of a typical flux feeding process. The left panel is the Atmospheric Imaging Assembly (AIA) 304 Å observation of the prominence; the right panel is the slice-time plot along the slit marked as "A" in the left panel. This figure is adapted from Zhang et al. (2014).

rising velocity of the prominence. Eventually, the prominence erupted. Therefore it was suggested that the eruption could be initiated by flux feeding processes. This also indicates that flux feeding could be regarded as one of the precursors of solar eruptions (e.g., Wang et al. 2017a). The physical nature of the flux rope eruptions initiated by flux feeding, however, remains unclear; there are still many issues about this scenario. The most prominent one is, why could flux feeding cause the prominence to erupt? Is this merely a coincidence or actually an indication of some physical mechanism? Moreover, there were three flux feeding episodes in the pre-eruptive phase of the prominence. Why did the prominence not erupt after the first and the second flux feeding episodes, but only erupt after the third one? Was it the three flux feeding episodes as a whole or only the third one that was responsible for the onset of the eruption? These questions could hardly be resolved based on observational results alone. Theoretical investigations are needed to shed light on the physical nature of the flux rope eruptions caused by flux feeding processes.

In this Letter, we carry out numerical simulations to investigate the physical nature of the flux rope eruption initiated by flux feeding. The major science question is about the influence of flux feeding processes on coronal flux rope systems, especially the role that flux feeding plays in the onset of the eruptions. The rest of the paper is arranged as follows: the simulating procedures are introduced in Section 2; simulation results of a typical flux feeding event are presented in Section 3; the physical nature of the onset of the eruptions is investigated in Section 4. Finally, our discussion and conclusion are given in Section 5.

2. Simulating Procedures

For 2.5-dimensional cases (with $\partial/\partial z = 0$) in Cartesian coordinates, the magnetic field can be denoted as

$$\boldsymbol{B} = \nabla\psi \times \hat{z} + B_z\hat{z}, \tag{1}$$

where ψ is the magnetic flux function and B_z is the component of $\boldsymbol{B}$ in the z-direction. Basic equations and procedures to obtain the initial state are introduced in the Appendix. The background field is a partially open bipolar field (Figure 2(a)). Anomalous resistivity is used here so that magnetic

reconnection is restricted within the region of current sheets:

$$\eta = \begin{cases} 0, & j \leqslant j_c \\ \eta_m \mu_0 v_0 L_0 \left(\frac{j}{j_c} - 1\right)^2. & j > j_c. \end{cases} \tag{2}$$

Here $\eta_m = 10^{-4}$ and $L_0 = 10^7$ m, and $v_0 = \sqrt{RT_0} = 128.57$ km s^{-1}, where $T_0 = 10^6$ K; $R = 1.65 \times 10^4$ J kg^{-1} K^{-1} is the specific gas constant and μ_0 is the vacuum magnetic permeability; the critical current density is $j_c = 2.37 \times 10^{-4}$ A m^{-2}.

The initial state is a stable equilibrium state (Figure 2(b)): a flux rope is embedded in the bipolar background field. In our simulation, the rising fibril in the scenario of flux feeding is represented by a small flux rope, which emerges from below the preexisting flux rope, then rises and interacts with the preexisting rope. For simplicity, the preexisting large flux rope is called the major flux rope hereafter. Assume that the small rope, whose radius is $a = 5$ Mm, begins to emerge at $t = 0$ in the central region of the base right below the major rope, and the emergence ends at $t = \tau_E = 30\tau_A$ s; $\tau_A = L_0^2\sqrt{\mu_0\rho_0}/\psi_0 = 17.4$ s is the characteristic Alfvén transit time, where $\rho_0 = 3.34 \times 10^{-13}$ kg m^{-3} and $\psi_0 = 3.73 \times 10^3$ Wb m^{-1}. With a constant emerging speed, the emerged part of the small rope at time t is located within $-x_E \leqslant x \leqslant x_E$, where

$$x_E = (a^2 - h_E^2)^{1/2}, \ h_E = a(2t/\tau_E - 1). \tag{3}$$

Based on this, the emergence of the small flux rope is achieved by adjusting ψ, B_z, velocities $v_{x,y,z}$, temperature T, and density ρ at the base of the emerged part of the small rope ($y = 0$, $-x_E \leqslant x \leqslant x_E$):

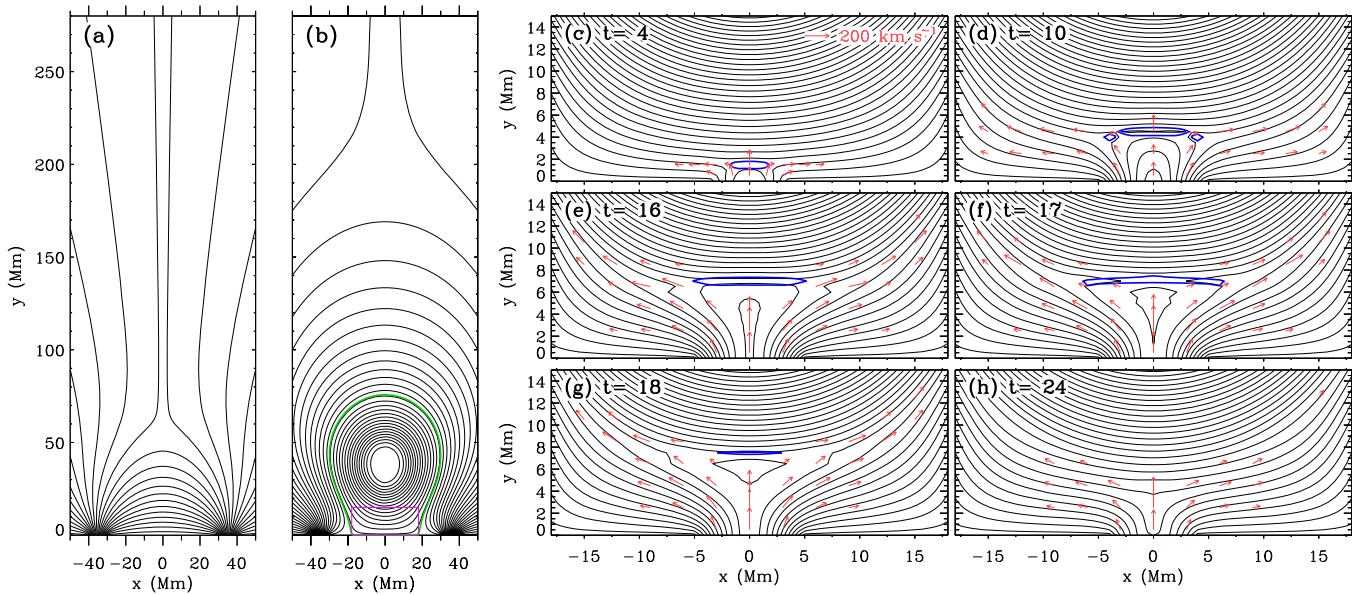$$\psi(t, x, y = 0) = \psi_i(x, y = 0) + \psi_E(t, x), \tag{4}$$

$$\psi_E(t, x) = \frac{C_E}{2} \ln\left(\frac{2a^2}{a^2 + x^2 + h_E^2}\right), \tag{5}$$

$$B_z(t, x, y = 0) = C_E a(a^2 + x^2 + h_E^2)^{-1}, \tag{6}$$

$$v_y(t, x, y = 0) = v_E = 2a/\tau_E,$$
$$v_x(t, x, y = 0) = v_z(t, x, y = 0) = 0, \tag{7}$$

$$T(t, x, y = 0) = 2 \times 10^5 \text{ K}, \ \rho(t, x, y = 0)$$
$$= 1.67 \times 10^{-12} \text{ kg m}^{-3}. \tag{8}$$

Figure 2. Simulation results of a flux feeding process with $C_E = 1.90$. Panels (a) and (b) show the magnetic configurations of the background field and the initial state, respectively; the green curve marks the boundary of the rope; the pink box represents the region illustrated in Panels (c)–(h). The black curves in panels (c)–(h) are the magnetic field lines; the blue curves are the contours of the current density $j = 5.63 \times 10^{-4}$ A m^{-2}. The red arrows illustrate the distribution of the velocity in the x–y plane; the length of arrows are proportional to the velocities; an example of 200 km s^{-1} is plotted in panel (c). The time is in units of τ_A.

Here ψ_i is the magnetic flux function of the initial state. Apart from during the emergence of the small rope, ψ at the base is fixed at ψ_i, so that it corresponds to the photosphere. B_z is positive and $\boldsymbol{B}_{xy}$ (the component of B in x–y plane) is counterclockwise in both the small and the major ropes. It is widely accepted that the distribution of coronal magnetic field plays a dominant role in how the eruption of a flux rope is triggered (e.g., Sun et al. 2012). Thus the influence of flux feeding on the major rope should be sensitive to the scale of the strength of magnetic field in the emerging small rope. As shown in Equations (5) and (6), the parameter C_E determines the magnetic field strength of the small rope; its dimensionless values quoted in the rest of the paper are given in units of $\psi_0 = 3.73 \times 10^3$ Wb m^{-1}. In our simulations, we change C_E to investigate the influences of different flux feeding processes on the major flux rope system. It should be noted that the science focus and simulating procedures in this work are quite different from those of Zhang et al. (2017b), in which the catastrophic behaviors of a single flux rope were investigated.

3. Simulation Results

The simulation result of a typical flux feeding process with $C_E = 1.90$ is shown in Figure 2. At the early stage of the flux feeding process, the emerging small flux rope appears below the major rope, as shown in Figure 2(c). A horizontal current sheet forms at the interface between the small and major ropes, as marked by the blue curves in Figure 2, which are the contours of the current density $j = 5.63 \times 10^{-4}$ A m^{-2}. The emerged small rope could be clearly recognized in Figure 2(g) and the corresponding distribution of B_x in Figure 3(e). As a result of the magnetic reconnection within the current sheet, the magnetic field lines of the small rope gradually reconnect with those of the major rope (see Figures 2(e)–(h)). The height of the current sheet gradually increases with time, triggering flows within the major rope, as illustrated by the red arrows in

Figures 2(e)–(h). Eventually, the two flux ropes merge together. Note that since the major rope sticks to the photosphere, the reconnection occurs immediately after the small rope begins to emerge. The topology of the resultant flux rope system after flux-feeding is shown in Figure 4(a).

Further evolution of the resultant flux rope system indicates that this flux feeding process with $C_E = 1.90$ eventually triggers the major rope to erupt. As shown in Figure 4(g), the eruption of the rope occurs after the flux feeding process. After the onset of the eruption, the lower boundary of the rope is not detached from the photosphere instantly, but keeps sticking to the photosphere for a certain period (Figures 4(b) and (c)). As the height of the rope increases, the lower part of the rope, along with the adjacent background field lines, are stretched, during which the flux rope is gradually accelerated. Eventually, a vertical current sheet forms beneath the flux rope, as shown in Figures 4(d)–(f). The magnetic reconnection that occurs in this current sheet should drive the further acceleration of the flux rope. The obvious delay of the appearance of this current sheet relative to the onset of the eruption indicates that the eruption should be triggered by an ideal process. This is consistent with the observations in Paper I, in which there was no intense heating around the source region of the prominence during the early period of its eruption, indicating that fast magnetic reconnection plays no crucial role in triggering the eruption. It is noteworthy that the initial state is a stable equilibrium: if there is no flux feeding process, the major rope will keep sticking to the photosphere forever.

4. Analysis

As shown in the simulations demonstrated in Section 3, flux feeding is able to eventually cause a flux rope system to erupt, consistent with the conclusion in Paper I. To further understand the physical nature of this scenario, detailed investigation about the influence of different settings of the flux feeding is needed. It has already been mentioned in Section 2 that C_E determines the magnetic field strength in the emerging small flux rope, so
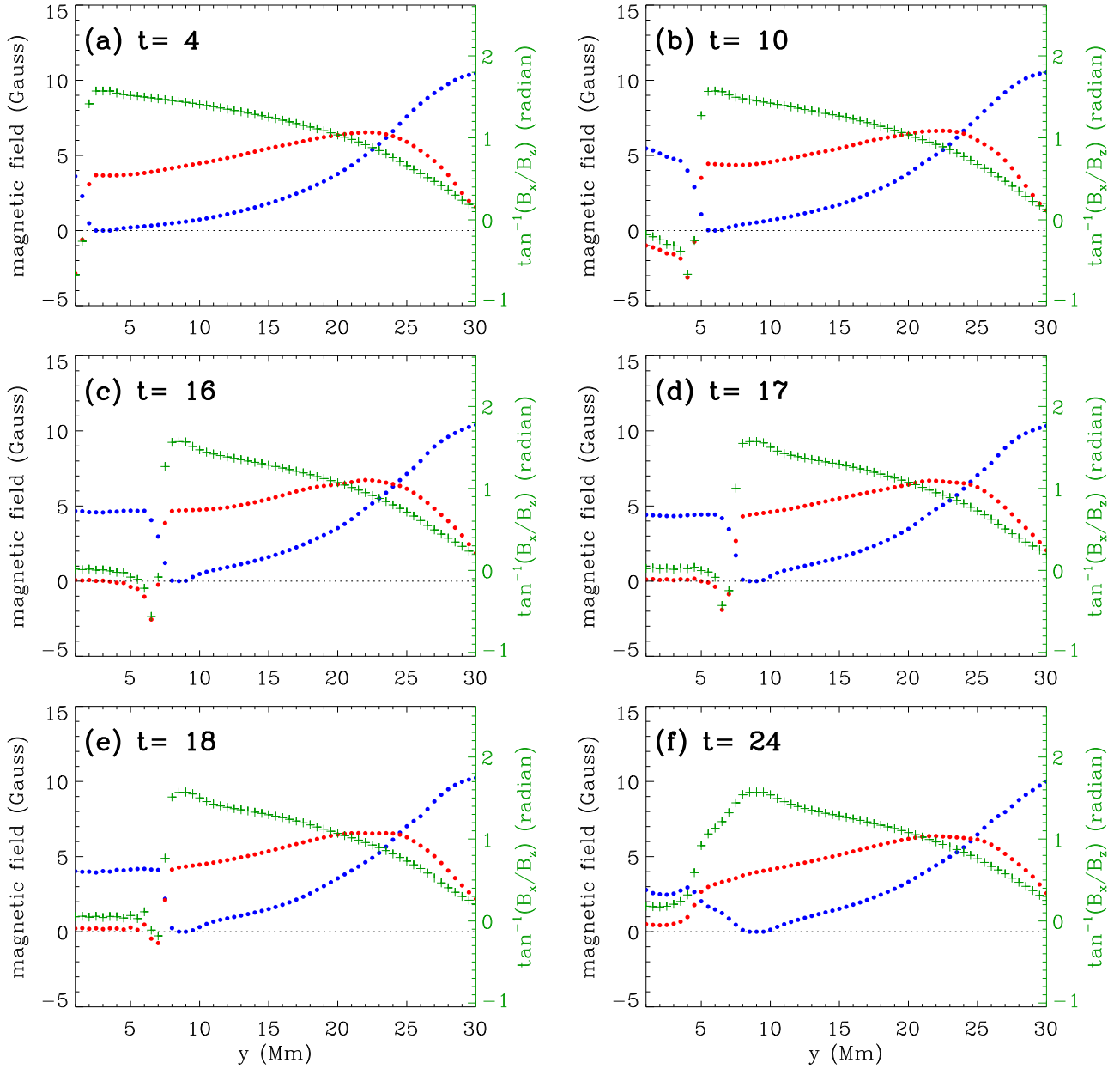
Figure 3. Distributions of B_x (red dots), B_z (blue dots), and $\tan^{-1}(B_x/B_z)$ (green plus signs) along $x = 0$ in the states shown in Figures 2(c)–(h). The black horizontal dotted lines represent $B = 0$. The time is in units of τ_A.

that cases with different C_E correspond to different intensities of flux feeding.

The properties of the major rope is characterized by the axial magnetic flux, Φ_z, and the poloidal magnetic flux per unit length along the z-direction, Φ_p. In the initial state shown in Figure 2(b), the axial flux $\Phi_{z0} = 9.31 \times 10^{19}\,\mathrm{Mx}$, the poloidal flux $\Phi_{p0} = 1.49 \times 10^{10}\,\mathrm{Mx\,cm^{-1}}$. Assuming the length of the rope is 100 Mm, the total poloidal flux of the flux rope is of the order $1.5 \times 10^{20}\,\mathrm{Mx}$. For the case with $C_E = 1.90$ shown in Section 3, the axial flux Φ_z of the resultant rope at $t = 30\tau_A$ increases to $11.73 \times 10^{19}\,\mathrm{Mx}$, whereas the poloidal flux Φ_p is still $1.49 \times 10^{10}\,\mathrm{Mx\,cm^{-1}}$, almost the same as the initial state. This indicates that the twist angle within the rope should decrease after flux feeding. Simulation results with other different C_E also comes to a similar conclusion, indicating that flux feeding processes only inject axial flux into the major rope. This is because the poloidal flux of the small rope is entirely

canceled out by the magnetic reconnection during its merging process with the major rope. The injected axial flux is mainly distributed near the boundary of the flux rope, which results in the current in this region after flux feeding (see Figure 4(a)).

The flux feeding process, however, is not always able to trigger the major flux rope to erupt; it requires a certain threshold. For the cases with different C_E, Φ_z of the resultant rope at $t = 30\tau_A$ is plotted in Figure 5(a); the noneruptive cases (i.e., the major rope keeps sticking to the photosphere after flux feeding) with different C_E are plotted in circles with different colors, while the eruptive ones are plotted in black solid dots. For the case with larger C_E, the magnetic field in the small emerging rope is stronger, so that more axial flux is injected. It is obvious in Figure 5(a) that Φ_z of the resultant rope in the eruptive cases is larger than that in the noneruptive ones. For each noneruptive case in Figure 5(a), through using the noneruptive state as the new pre-feeding state, we let a new
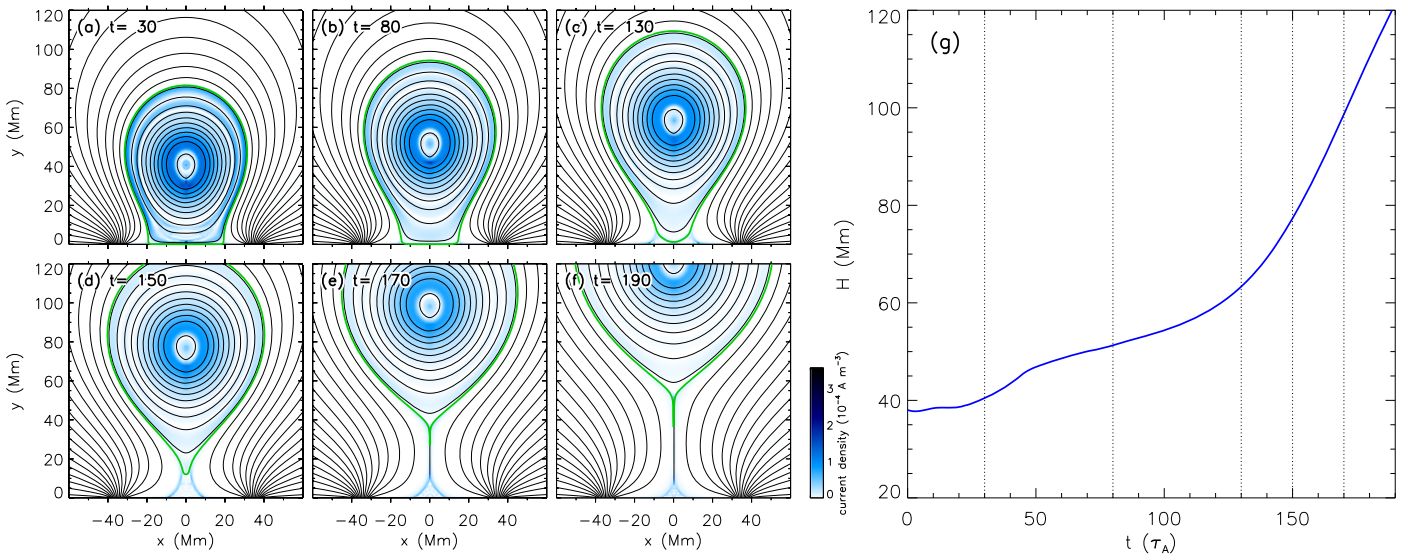
Figure 4. Eruptive process of the case with $C_E = 1.90$. The blue curve in panel (g) is the evolutionary profile of the height of the rope axis, H. Panels (a)–(f) show central sections of the domain during the evolution, in which the blue color depicts the distribution of the current density, and the green curves mark the boundary of the rope. The corresponding times of the states shown in panels (a)–(h) are marked by the vertical dotted lines in panel (g).

small rope emerge from below the major rope, and these cases are called the second round of flux feeding; the corresponding Φ_z at $t = 30\tau_A$ is plotted in Figure 5(b), and their colors are the same as their corresponding pre-feeding states. Similarly, the noneruptive cases are plotted in circles, and eruptive cases in dots. For clarification, the cases starting from the initial state in Figure 5(a) are called the first round. It is demonstrated in Figure 5 that the eruptive and noneruptive cases are separated. There should exist a critical value Φ_{zc} of the order 1.2×10^{20} Mx. If $\Phi_z < \Phi_{zc}$ (circles), the eventual height of the major rope is finite, whereas if $\Phi_z \geqslant \Phi_{zc}$ (dots), the eventual height should be infinite.

5. Discussion and Conclusion

In this Letter, we have carried out MHD numerical simulations to investigate the effect of flux feeding on coronal flux rope systems. In our simulations, it is found that the flux feeding processes only inject axial magnetic flux into the major rope, whereas the poloidal magnetic flux of the rope remains almost unchanged. The physical scenario of the eruption caused by flux feeding is by injecting axial flux into a flux rope in an incremental and intermittent fashion, flux feeding effectively drives the rope to evolve toward a critical condition and eventually can trigger its eruption. Therefore, our simulation results corroborate that flux feeding is a viable mechanism to cause the eruption of solar magnetic flux ropes. For the major flux rope, there exists a threshold Φ_{zc}: if the major rope's axial flux Φ_z is below Φ_{zc}, it will keep sticking to the photosphere, no matter how many flux feeding episodes have occurred; on the other hand, if Φ_z exceeds Φ_{zc}, the rope system will erupt.

The existence of the threshold Φ_{zc} indicates that the number of flux-feeding episodes is not important; only when the amount of its axial flux exceeds the critical value will the major rope erupt. Based on this result, the evolution of the observational event analyzed in Paper I can be interpreted as follows. The injected axial magnetic flux via the first and second observed flux feeding episodes might not be sufficient for the flux rope embedding the prominence to reach its critical

state, thus the prominence remained in a quasi-equilibrium (slow-rising) state. But the third episode of flux feeding became the "last straw," so that the flux rope erupted. The early flux feeding processes might not trigger the eruption, but with each episode of flux feeding the rope system was one step closer to the eruption.

As introduced in Section 1, previous studies suggested the presence of a critical axial flux for flux ropes; a catastrophe occurs if this critical value is reached. Our simulation results also support this theoretical conclusion. In the eruptions caused by flux feeding, the flux feeding processes continually inject axial flux, acting as a build-up toward the onset of the eruption. When the critical axial flux is reached, an upward catastrophe is triggered, and the further evolution of the upward catastrophe, along with the magnetic reconnection within the current sheet below the rope, drives the eruption of the flux rope (see Green et al. 2018 for the classification of "trigger" and "driver" for solar eruptions). The critical value in our simulation is of the order 1.2×10^{20} Mx, which is comparable with both the derived values in theoretical analyses (e.g., Su et al. 2011; Zhang et al. 2017b) and the observed magnetic fluxes of CMEs (e.g., Qiu et al. 2007; Hu et al. 2015; Wang et al. 2015, 2017b; Gopalswamy et al. 2017). The increase of Φ_z in the theoretical studies mentioned above is artificial, i.e., the discovered upward catastrophe is only a phenomenon in the parameter space of Φ_z, not reflecting the dynamic evolution of the system. The flux rope eruption in the corona, however, is a dynamic phenomenon in the physical space. Our simulations demonstrate flux feeding as a viable mechanism to prepare a flux rope for the upward catastrophe in the physical space, not just in the parameter space. It is noteworthy that, because of the different initial states and simulating procedures, the critical axial fluxes in, e.g., Zhang et al. (2017b), are not exactly the same as ours, and the rope systems eventually reach equilibria in that study.
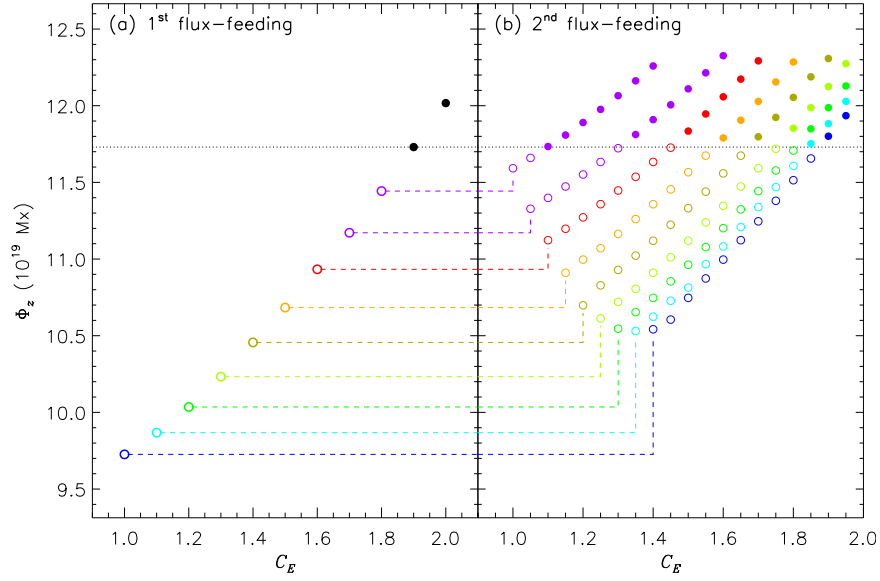
Figure 5. Total axial flux Φ_z of the resultant rope at $t = 30\tau_A$ for different C_E. The eruptive cases are plotted in solid dots, and noneruptive cases are plotted in circles. Panel (a) shows Φ_z of the resultant rope after the first round of flux feeding, and noneruptive cases with different C_E are in different colors. Panel (b) shows Φ_z after the second round, and their colors are the same as their corresponding pre-feeding states. The dashed lines do not have many physical implications, but mark the correspondence between the pre- and post-feeding states.

Appendix
Basic Equations and Initial Preparations

Through using Equation (1), the 2.5-dimensional MHD equations can be rewritten in dimensionless form as follows:

$$\frac{\partial \rho}{\partial t} + \nabla \cdot (\rho v) = 0, \tag{A1}$$

$$\frac{\partial v}{\partial t} + v \cdot \nabla v + \nabla T + \frac{T}{\rho}\nabla \rho$$
$$+ \frac{2}{\rho \beta_0}(\triangle \psi \nabla \psi + B_z \nabla B_z + \nabla \psi \times \nabla B_z) + g\hat{y} = 0, \tag{A2}$$

$$\frac{\partial \psi}{\partial t} + v \cdot \nabla \psi - \frac{2\eta}{\beta_0} \triangle \psi = 0, \tag{A3}$$

$$\frac{\partial B_z}{\partial t} + \nabla \cdot (B_z v) + (\nabla \psi \times \nabla v_z) \cdot \hat{z} - \frac{2\eta}{\beta_0} \triangle B_z = 0, \tag{A4}$$

$$\frac{\partial T}{\partial t} + v \cdot \nabla T + (\gamma - 1)T\nabla \cdot v$$
$$- \frac{4\eta(\gamma - 1)}{\rho R \beta_0^2}[(\triangle \psi)^2 + |\nabla \times (B_z \hat{z})|^2] = 0, \tag{A5}$$

where

$$\triangle \psi = \frac{\partial^2 \psi}{\partial x^2} + \frac{\partial^2 \psi}{\partial y^2}, \quad \triangle B_z = \frac{\partial^2 B_z}{\partial x^2} + \frac{\partial^2 B_z}{\partial y^2}, \tag{A6}$$

and ρ and T denote the density and the temperature; v_x, v_y, and v_z represent the x-component, y-component, and z-component of the velocity, respectively; γ is the polytropic index, which is selected to be $5/3$ in our simulation; g is the normalized gravity; and η is the resistivity. Here $\beta_0 = 2\mu_0\rho_0 RT_0L_0^2/\psi_0^2 = 0.1$ is the characteristic ratio of the gas pressure to the magnetic pressure, where $\rho_0 = 3.34 \times 10^{-13}\,\mathrm{kg\,m^{-3}}$, $T_0 = 10^6\,\mathrm{K}$, $L_0 = 10^7\,\mathrm{m}$, and $\psi_0 = 3.73 \times 10^3\,\mathrm{Wb\,m^{-1}}$ are the characteristic values of density, temperature, length, and magnetic flux function, respectively, which are also the calculating units in the simulation. The characteristic values of other quantities are $v_0 = 128.57\,\mathrm{km\,s^{-1}}$, $t_0 = 77.8\,\mathrm{s}$, $B_0 = 3.37 \times 10^{-4}\,\mathrm{T}$, and $g_0 = 1.65 \times 10^3\,\mathrm{m\,s^{-2}}$. The numerical domain is $0 < x < 200$ Mm, $0 < y < 300$ Mm, and discretized into 400×600 uniform meshes with grid spacing $\triangle x = \triangle y = 0.5$ Mm. Symmetric boundary condition is used for the left side ($x = 0$). The radiation and the heat conduction in the energy equation are neglected.

In order to investigate the influence of flux feeding on flux rope systems, we must first construct a typical coronal flux rope system, and then realize the flux feeding process in simulations. Here we select a partially open bipolar field, with negative and positive surface magnetic charges located at the photosphere within $-b < x < -a$ and $a < x < b$, respectively, as the background field, which can be obtained by the complex variable method (e.g., Hu et al. 1995; Zhang et al. 2017b). The background magnetic field can be cast in the complex variable form

$$f(\omega) \equiv B_x - iB_y$$
$$= \frac{(\omega + iy_N)^{1/2}(\omega - iy_N)^{1/2}}{F(a, b, y_N)} \ln\left(\frac{\omega^2 - a^2}{\omega^2 - b^2}\right), \tag{A7}$$

where $\omega = x + iy$, and

$$F(a, b, y_N) = \frac{1}{b-a} \int_a^b (x^2 + y_N^2)^{1/2} dx$$
$$= \frac{1}{2(b-a)} \times [b(b^2 + y_N^2)^{1/2} - a(a^2 + y_N^2)^{1/2}$$
$$+ y_N^2 \ln\left(\frac{b + (b^2 + y_N^2)^{1/2}}{a + (a^2 + y_N^2)^{1/2}}\right)]. \tag{A8}$$

Here $a = 30$ Mm, $b = 40$ Mm, and $(y = y_N = 60.6$ Mm, $x = 0)$ is the position of the neutral point of the partially open bipolar field. The neutral current sheet of the background field is located at $(x = 0, \ y \geqslant y_N)$. The width of the surface magnetic charges is $w = b - a = 10$ Mm, and the distance between them is $d = 2a = 60$ Mm. The magnetic flux function could then be calculated by:

$$\psi(x, y) = \text{Im}\left\{\int f(\omega)d\omega\right\}, \tag{A9}$$

and the flux function at the lower base is

$$\psi_i(x, 0) = \begin{cases} \psi_c, & |x| < a \\ \psi_c F(|x|, b, y_N)/F(a, b, y_N), & a \leqslant |x| \leqslant b \\ 0, & |x| > b \end{cases} \tag{A10}$$

where $\psi_c = \pi\psi_0$; the flux function at the neutral point $y = y_N$ is

$$\psi_N = \frac{\pi(b^2 - a^2)}{2F(a, b, y_N)}. \tag{A11}$$

The background field is potential everywhere except along the neutral current sheet and at the lower base. For potential magnetic fields, $f(\omega) = B_x - iB_y$ satisfies the Cauchy−Riemann condition, so that the integral in Equation (A9) is independent of the integration path in as far as the integration path does not touch the neutral current sheet and the lower base. The flux function along the neutral current sheet of the background partially open bipolar field is a constant, which is given by Equation (A11); the flux function at the lower base is given by Equation (A10). With the flux function calculated above, and let B_z equals 0 in the background field, the configuration of the background field is obtained, as shown in Figure 2(a). The reconnection in the current sheet of the background field is prohibited by the method introduced in Hu et al. (2003). The initial corona is isothermal and static with

$$T_c \equiv T(0, x, y) = 1 \times 10^6 \text{ K}, \ \rho_c \equiv \rho(0, x, y) = \rho_0 e^{-gy}. \tag{A12}$$

As mentioned above, symmetric condition used at the left boundary. Except during the emergence of the small rope, the lower boundary is fixed: the flux function ψ is fixed at ψ_i given by Equation (A10); B_z is fixed at 0; the velocity at the lower boundary is zero; the density and the temperature are fixed at their initial values, which are given by Equation (A12). The quantities at the right and top boundaries are evaluated by

increment equivalent extrapolations (e.g., Hu & Liu 2000):

$$U_b^{n+1} = U_{b-1}^{n+1} + U_b^n - U_{b-1}^n.$$

Here U represents the quantities (e.g., ρ, $\mathbf{v}$, and ψ); the superscript n and n + 1 indicates the quantities at the current and the next time steps, respectively; U_b represents the quantities at the boundary, and U_{b-1} the quantities at the location next to the boundary. The boundary quantities at the next time step, U_b^{n+1}, are then prescribed.

With the initial and background conditions, Equations (A1)–(A5) are simulated by the multistep implicit scheme (Hu 1989). Starting from the background field, first by letting a flux rope emerge from the lower base, we obtain a flux rope system with the rope sticking to the photosphere; then adjust the axial and poloidal fluxes of the rope to $\Phi_{z0} = 9.31 \times 10^{19}$ Mx and $\Phi_{p0} = 1.49 \times 10^{10}$ Mx cm^{-1}, respectively, and let the rope system relax to a stable equilibrium state. The relaxation is achieved by letting the rope system evolve for a long enough time, during which the fluxes of the rope are fixed at Φ_{z0} and Φ_{p0}; as a result of the numerical diffusion in the simulation, the rope system eventually reaches an equilibrium state. The final equilibrium state is just the initial state of our simulation (as shown in Figure 2(b)), and the rope with $\Phi_z = \Phi_{z0}$ and $\Phi_p = \Phi_{p0}$ in this state is the so-called major flux rope. This flux rope system is in a bald patch separatrix configuration. Note that the radius of the flux rope is finite here, i.e., there is no constraint on the ratio of the radius to, e.g., the characteristic photospheric length, so that the initial state could not be derived by analytical methods but could only be obtained by numerical procedures.

ORCID iDs

Quanhao Zhang ⓘ https://orcid.org/0000-0003-0565-3206
Yuming Wang ⓘ https://orcid.org/0000-0002-8887-3919
Rui Liu ⓘ https://orcid.org/0000-0003-4618-4979
Jie Zhang ⓘ https://orcid.org/0000-0003-0951-2486
Bin Zhuang ⓘ https://orcid.org/0000-0002-5996-0693

References

Antiochos, S. K., DeVore, C. R., & Klimchuk, J. A. 1999, ApJ, 510, 485
Archontis, V., & Hood, A. W. 2008, ApJL, 674, L113
Aulanier, G., Török, T., Démoulin, P., & DeLuca, E. E. 2010, ApJ, 708, 314
Berger, T. E., Slater, G., Hurlburt, N., et al. 2010, ApJ, 716, 1288
Bobra, M. G., van Ballegooijen, A. A., & DeLuca, E. E. 2008, ApJ, 672, 1209
Chen, P. F., & Shibata, K. 2000, ApJ, 545, 524
Chen, Y., Hu, Y. Q., & Sun, S. J. 2007, ApJ, 665, 1421
Cheng, X., Ding, M. D., Zhang, J., et al. 2014, ApJ, 789, 93
Démoulin, P., & Aulanier, G. 2010, ApJ, 718, 1388
Fan, Y., & Gibson, S. E. 2007, ApJ, 668, 1232
Forbes, T. G., & Isenberg, P. A. 1991, ApJ, 373, 294
Gopalswamy, N., Yashiro, S., Akiyama, S., & Xie, H. 2017, SoPh, 292, 65
Green, L. M., Török, T., Vršnak, B., Manchester, W., & Veronig, A. 2018, SSRv, 214, 46
Guo, Y., Ding, M. D., Schmieder, B., et al. 2010, ApJL, 725, L38
Hu, Q., Qiu, J., & Krucker, S. 2015, JGRA, 120, 5266
Hu, Y. Q. 1989, JCoPh, 84, 441
Hu, Y. Q., Li, G. Q., & Xing, X. Y. 2003, JGRA, 108, 1072
Hu, Y. Q., Li, X., & Ai, G. X. 1995, ApJ, 451, 843
Hu, Y. Q., & Liu, W. 2000, ApJ, 540, 1119
Inoue, S., Hayashi, K., Magara, T., Choe, G. S., & Park, Y. D. 2015, ApJ, 803, 73
Isenberg, P. A., Forbes, T. G., & Demoulin, P. 1993, ApJ, 417, 368
Jiang, C., Feng, X., & Hu, Q. 2018, ApJ, 866, 96
Kliem, B., Lin, J., Forbes, T. G., Priest, E. R., & Török, T. 2014a, ApJ, 789, 46
Kliem, B., & Török, T. 2006, PhRvL, 96, 255002

Kliem, B., Török, T., Titov, V. S., et al. 2014b, ApJ, 792, 107

Lin, J., & Forbes, T. G. 2000, JGR, 105, 2375

Lin, J., Forbes, T. G., & Isenberg, P. A. 2001, JGR, 106, 25053

Liu, R., Kliem, B., Török, T., et al. 2012, ApJ, 756, 59

Longcope, D. W., & Forbes, T. G. 2014, SoPh, 289, 2091

Moore, R. L., Sterling, A. C., Hudson, H. S., & Lemen, J. R. 2001, ApJ, 552, 833

Qiu, J., Hu, Q., Howard, T. A., & Yurchyshyn, V. B. 2007, ApJ, 659, 758

Romano, P., Contarino, L., & Zuccarello, F. 2003, SoPh, 214, 313

Savcheva, A. S., van Ballegooijen, A. A., & DeLuca, E. E. 2012, ApJ, 744, 78

Shen, F., Shen, C., Zhang, J., et al. 2014, JGRA, 119, 7128

Sterling, A. C., & Moore, R. L. 2004, ApJ, 602, 1024

Su, Y., Surges, V., van Ballegooijen, A., DeLuca, E., & Golub, L. 2011, ApJ, 734, 53

Su, Y., van Ballegooijen, A., Lites, B. W., et al. 2009, ApJ, 691, 105

Sun, X., Hoeksema, J. T., Liu, Y., et al. 2012, ApJ, 748, 77

Török, T., & Kliem, B. 2003, A&A, 406, 1043

van Driel-Gesztelyi, L., & Green, L. M. 2015, LRSP, 12, 1

Wang, H., Liu, C., Ahn, K., et al. 2017a, NatAs, 1, 0085

Wang, W., Liu, R., Wang, Y., et al. 2017b, NatCo, 8, 1330

Wang, Y., Zhou, Z., Shen, C., Liu, R., & Wang, S. 2015, JGRA, 120, 1543

Yan, X. L., Wang, J. C., Pan, G. M., et al. 2018, ApJ, 856, 79

Zhang, J., Dere, K. P., Howard, R. A., Kundu, M. R., & White, S. M. 2001, ApJ, 559, 452

Zhang, Q., Liu, R., Wang, Y., et al. 2014, ApJ, 789, 133

Zhang, Q., Wang, Y., Hu, Y., et al. 2017a, ApJ, 851, 96

Zhang, Q., Wang, Y., Hu, Y., & Liu, R. 2016, ApJ, 825, 109

Zhang, Q., Wang, Y., Hu, Y., Liu, R., & Liu, J. 2017b, ApJ, 835, 211

Zhuang, B., Hu, Y., Wang, Y., et al. 2018, JGRA, 123, 2513